



**HAL**  
open science

# Paramagnetic properties of $[An IV (NO_3)_6]^{2-}$ Complexes ( $An = U, Np, Pu$ ) probed by NMR spectroscopy and quantum chemical calculations

Matthieu Autillo, Marie-Claire Illy, Luca Briscese, Md. Ashraful Islam, H el ene Bolvin, Claude Berthon

► **To cite this version:**

Matthieu Autillo, Marie-Claire Illy, Luca Briscese, Md. Ashraful Islam, H el ene Bolvin, et al.. Paramagnetic properties of  $[An IV (NO_3)_6]^{2-}$  Complexes ( $An = U, Np, Pu$ ) probed by NMR spectroscopy and quantum chemical calculations. *Inorganic Chemistry*, 2024, 63, pp.12969-12980. 10.1021/acs.inorgchem.4c01694 . hal-04687575

**HAL Id: hal-04687575**

**<https://hal.science/hal-04687575v1>**

Submitted on 21 Nov 2024

**HAL** is a multi-disciplinary open access archive for the deposit and dissemination of scientific research documents, whether they are published or not. The documents may come from teaching and research institutions in France or abroad, or from public or private research centers.

L'archive ouverte pluridisciplinaire **HAL**, est destin ee au d ep ot et  a la diffusion de documents scientifiques de niveau recherche, publi es ou non,  emanant des  tablissements d'enseignement et de recherche fran ais ou  trangers, des laboratoires publics ou priv es.

# Paramagnetic properties of $[\text{An}^{\text{IV}}(\text{NO}_3)_6]^{2-}$ complexes (An = U, Np, Pu) probed by NMR spectroscopy and quantum chemical calculations.

Matthieu Autillo <sup>†</sup>, Marie-Claire Illy <sup>‡</sup>, Luca Briscese <sup>‡</sup>, Md. Ashraful Islam <sup>§</sup>,  
Hélène Bolvin <sup>¶\*</sup>, Claude Berthon <sup>‡\*</sup>

<sup>†</sup>CEA, DES, ISEC, DPME, Univ. Montpellier, Bagnols/Cèze 30207, France.

<sup>‡</sup>CEA, DES, ISEC, DMRC, Univ. Montpellier, Bagnols/Cèze 30207, France.

<sup>§</sup>Centre de Résonance Magnétique Nucléaire à Très Hauts Champs - CRMN, 5 Rue de la Doua, 69100 Villeurbanne, France.

<sup>¶</sup>Laboratoire de Chimie et Physique Quantiques, CNRS, Université Toulouse III, 118 route de Narbonne, 31062 Toulouse, France.

\* e-mail addresses: claud.berthon@cea.fr; bolvin@irsamc.ups-tlse.fr

## Abstract

Actinide +IV complexes with six nitrates  $[\text{An}^{\text{IV}}(\text{NO}_3)_6]^{2-}$  (An = Th, U, Np and Pu) have been studied by  $^{15}\text{N}$  and  $^{17}\text{O}$  NMR spectroscopies in solution and first principles calculations. Magnetic susceptibilities were evaluated experimentally using Evans method and are in good agreement with the ab initio values. The evolution in the series of the crystal field parameters deduced from ab initio calculations is discussed. The NMR paramagnetic shifts are analyzed based on ab initio calculations. Since the cubic symmetry of the complex quenches the dipolar contribution, they are only of Fermi contact origin. They are evaluated from first principles based on a CAS/DFT strategy, in good accordance with the experimental one. The ligands hyperfine coupling constants are deduced from paramagnetic shifts and calculated using unrestricted DFT. The latter are decomposed in terms of the contribution of molecular orbitals. It highlights two pathways for the delocalization of the spin density from the metallic open-shell  $5f$  orbitals to the NMR active nuclei, either through the valence  $5f$  hybridized with  $6d$  to the valence  $2p$  molecular orbitals of the ligands, or by spin polarization of the metallic  $6p$  orbitals which interact with the  $2s$  based molecular orbitals of the ligands.

## Introduction

The physicochemical properties of actinide (An) cations have been the subject of numerous researches to better characterize and understand the ligand-actinide bonding character driving their chemical behavior.<sup>1,2</sup> A particular interest may be focused on the magnetic properties study of these elements in order to obtain information on unpaired  $5f$  electrons and their role in the An bonding properties. Because of their peculiar electronic structure, the An chemistry is strongly complicated by the possibility to stabilize various oxidation states (from +III to +VII).<sup>3</sup> Both for the industrial interest of the An(III) / Ln(III) separation and for the quest for heavy actinides, most analysis of the covalent effects were carried out on An(III) cations.<sup>4-8</sup> On the other hand, very few studies have investigated the covalent nature of the An(IV)-ligand bond due to the strong electrostatic component<sup>8-14</sup> and experimental constraints required to handle such radioactive elements.<sup>7, 15-22</sup>

We recently studied the  $\text{An}^{\text{IV}}$ -DPA (An = Th, U, Np and Pu, DPA = dipicolinate) series<sup>14</sup> and showed that pNMR (paramagnetic Nuclear Magnetic Resonance) provides interesting information on the bonding in comparison to the  $\text{An}^{\text{III}}$ -DPA (An = Pu, Am, Cm) series.<sup>23</sup> pNMR shifts arise from contact and dipolar contributions<sup>a</sup>. The first one contains information related to the electronic spin delocalization from the metal center to a nucleus while the second one is a through space magnetic interaction and contains structural information. The separation of both contributions is often a bottleneck. In lanthanide complexes, the different temperature dependence of the two terms has been widely used<sup>25</sup> but this method has shown limitations when applied to actinide complexes where the metal-ligand interaction is more important.<sup>26</sup> On one hand, the contact term is larger due to larger covalent interaction and on the other hand, the dipolar term is more entangled because the splitting of ground term of the free ion  $J$  is much larger

<sup>a</sup>This partition is valid in the non-relativistic limit<sup>24</sup>

than room temperature.<sup>27</sup>

Of primary interest are the examples where one of the contribution is dominant. It is the case for the dipolar contribution when the complex is highly anisotropic, as for actinyl complexes<sup>28–32</sup> or for <sup>1</sup>H far away from the paramagnetic center.<sup>14,33</sup> Conversely, contact interactions prevail for nuclei close to the paramagnetic center or for highly symmetric complexes where the magnetic anisotropy is weak.<sup>17,34</sup> It was the case for the An<sup>IV</sup>-DPA series where the coordination is very compact and the contact was dominant but the dipolar term not vanishing. In this work, we probe the paramagnetic properties of the [An<sup>IV</sup>(NO<sub>3</sub>)<sub>6</sub>]<sup>2-</sup> (An = Th, U, Np, Pu) complexes using pNMR for <sup>15</sup>N and <sup>17</sup>O nuclei and CAS (Complete Active Space) based and DFT (Density Functionnal Theory) calculations. We take advantage of the high symmetry of the [An<sup>IV</sup>(NO<sub>3</sub>)<sub>6</sub>]<sup>2-</sup> complexes structure, which quenches the dipolar contribution, to get a better insight in An<sup>IV</sup> (Th, U, Np and Pu) covalent properties.

## Experimental and Computational Section

### Experimental Section

**Synthesis.** Caution!!! <sup>232</sup>Thorium, <sup>238+235</sup>Uranium, <sup>237</sup>Neptunium and <sup>239+240</sup>Plutonium are radioactive elements and have to be handled in dedicated facilities with appropriate equipment for radioactive materials. Their manipulation has been carried out at the ATALANTE facility (CEA-Marcoule, France). The experiments involving Np and Pu were performed in a regular air atmosphere negative pressure glove box with restrictive protocols, whereas Th and U were manipulated under fume hood. Tetraethylammonium nitrate ((C<sub>2</sub>H<sub>5</sub>)<sub>4</sub>NNO<sub>3</sub>) (noted TEA nitrate hereafter), HNO<sub>3</sub> 70%, *tert*-Butyl alcohol (*t*-BuOH) and tetrahydrofuran (THF) were purchased from Sigma-Aldrich and used as received. CD<sub>3</sub>CN from Merck (ref. 366544) contains 0.03% of TMS and less than 200ppm of water. In order to perform <sup>15</sup>N and <sup>17</sup>O NMR spectra, enriched H<sup>15</sup>NO<sub>3</sub> (Aldrich, 98 atom % <sup>15</sup>N at ≈ 10 mol.L<sup>-1</sup>) and H<sub>2</sub><sup>17</sup>O (Cambridge Isotope, with 6.8, 90.8 and 2.4 atom % of <sup>16</sup>O, <sup>17</sup>O and <sup>18</sup>O respectively) were used.

**Preparation of <sup>17</sup>O doped TEA nitrate.** A stock solution is prepared by dissolving about 400 mg of the TEA nitrate commercial compound in 400 μL of H<sub>2</sub><sup>17</sup>O with 10 μL of the 10 mol.L<sup>-1</sup> H<sup>15</sup>NO<sub>3</sub> and leaved for a few days at 60°C in an oven. <sup>17</sup>O NMR performed on this solution revealed about 21% <sup>17</sup>O enrichment.

**Preparation of [(C<sub>2</sub>H<sub>5</sub>)<sub>4</sub>N]<sub>2</sub>An<sup>IV</sup>(<sup>15</sup>N<sup>17</sup>O<sub>3</sub>)<sub>6</sub>.** The An<sup>IV</sup> solid compounds were synthesized according to the method already reported.<sup>22</sup> An<sup>IV</sup> starting solutions were prepared in 2 mol.L<sup>-1</sup> H<sup>15</sup>NO<sub>3</sub> by dissolution of An<sup>IV</sup> hydroxide compounds freshly precipitated. Two equivalents of <sup>17</sup>O enriched TEA nitrate is added to the An<sup>IV</sup> <sup>15</sup>N nitrate samples and placed under nitrogen gas to improve the amount of precipitate. The solid is washed twice with 200 μL of tetrahydrofuran to remove nitric acid excess and dried under nitrogen gas. Finally the resulting powder is dissolved in CD<sub>3</sub>CN for NMR analysis. <sup>1</sup>H NMR spectra are performed to check that water is in sufficiently small amount to avoid nitrate site exchanges.

**NMR spectroscopy.** <sup>1</sup>H, <sup>15</sup>N and <sup>17</sup>O NMR spectra were recorded using a 400 MHz Fourier transform spectrometer, Agilent DD2, set up for the study of radioactive samples.<sup>15</sup> Acquisitions and processing were performed with OpenVnmrJ 2.1A software (Available at: <http://github.com/OpenVnmrJ>). Acquisition of <sup>17</sup>O spectra is performed with a standard pulse sequence (delay-pulse-acquisition). Baseline distortion is canceled using backward-linear processing over the 15 first points of the FID (Free Induction Decay). <sup>1</sup>H and <sup>15</sup>N spectra refer to water and nitromethane reference scales respectively. The plots of stacked spectra are performed with MestReNova 14.2 software as well as the determination of peak positions as a function of temperature.

The molar magnetic susceptibilities  $\chi_M^{exp}$  (in m<sup>3</sup>.mol<sup>-1</sup>) of the samples were deduced with the Evans method<sup>35</sup> according to

$$\chi_M^{exp} = \frac{3\Delta\delta}{10^3 [\text{An}^{\text{IV}}]} \quad (1)$$

where  $\Delta\delta$  is the dimensionless chemical shift difference between the <sup>1</sup>H NMR signals of working (*t*-BuOH<sub>in</sub>) and reference (*t*-BuOH<sub>out</sub>) solutions, [An<sup>IV</sup>] is the molar concentration (mol.L<sup>-1</sup>) of the paramagnetic element and  $\chi_M$  is the molar magnetic susceptibility. The *t*-BuOH concentration was 0.1 mol.L<sup>-1</sup>. The uncertainty values were estimated by taking into account the  $\Delta\delta$  precision of the NMR spectra (about 1%) and concentration measurements from UV-vis spectra and alpha counting (about 5%).

**UV-visible spectrophotometry.** The [(C<sub>2</sub>H<sub>5</sub>)<sub>4</sub>N]<sub>2</sub>An<sup>IV</sup>(NO<sub>3</sub>)<sub>6</sub> solid compounds dissolved in CD<sub>3</sub>CN were analyzed by UV-visible absorption spectroscopy using a Cary 5000 UV spectrophotometer (Agilent).

The UV-visible spectra of [Pu<sup>IV</sup>(NO<sub>3</sub>)<sub>6</sub>]<sup>2-</sup> complex were already recorded by Ryan *et al.* then Reilly *et al.* after dissolution of the corresponding alkylammonium salt in CH<sub>3</sub>CN solution.<sup>36,37</sup> A conservation of the Pu coordination sphere in

the  $[\text{Pu}^{\text{IV}}(\text{NO}_3)_6]^{2-}$  anion in solution were associated to the similarities with  $\text{Pu}^{\text{IV}}$  solutions in concentrated nitric acid or loaded on anion exchange resin<sup>36</sup> while for the solid state, spectrum had quite different features.<sup>37</sup> A comparison of the UV-visible spectra of  $[(\text{C}_2\text{H}_5)_4\text{N}]_2\text{An}^{\text{IV}}(\text{NO}_3)_6$  dissolved in  $\text{CD}_3\text{CN}$  and in concentrated  $\text{HNO}_3$  reveals also very similar feature that confirms the conservation of the  $[\text{An}^{\text{IV}}(\text{NO}_3)_6]^{2-}$  complexes in  $\text{CD}_3\text{CN}$  solution (see Figure S2).

## Computational details

Calculations were performed on the XRD structures<sup>22,38,39</sup> symmetrized to the  $\mathcal{T}_h$  symmetry. The coordinates are given in Table S1. For the sake of comparison, some calculations were performed using the XRD structures. When not specified, the results are given for the  $\mathcal{T}_h$  structure. Geometry optimization were previously performed<sup>22</sup>

**WFT Calculations.** MOLCAS calculations were performed with the version 8.<sup>40</sup> ANO-RCC basis sets of TZP quality were used. Firstly, Spin-Free Complete-Active-Space Self Consistent-Field (SF-CASSCF) calculations were performed<sup>41</sup> with an active space composed of the seven 5f orbitals of the actinide ion, and associated electrons, i.e. CAS(n,7). For  $\text{U}^{\text{IV}}$ , 21 triplets and 27 singlets are considered, for  $\text{Np}^{\text{IV}}$  30 quartets and 43 doublets, and for  $\text{Pu}^{\text{IV}}$  30 quintets, 73 triplets and 17 singlets. Dynamical correlation is added using the Complete-Active-Space Perturbation-Theory at 2nd order (CASPT2) method<sup>42</sup> with a level shift of 0.1 a.u.. Relativistic effects were taken into account by means of the Douglas-Kroll-Hess transformation<sup>43</sup> and Spin-Orbit (SO) integrals are calculated using the AMFI (Atomic Mean-Field Integrals) approximation.<sup>44</sup> SO coupling is included by a state interaction with the RASSI (Restricted Active Space State Interaction) method;<sup>45</sup> the state interaction is calculated between the CASSCF wave functions with CASSCF energies or Single-State CASPT2 energies leading to SO-CASSCF and SO-CASPT2 results, respectively. Some results are given restricting the SO calculations to only states with the same spin as the ground state,  $S_{max}$ . The magnetic susceptibility and its spin-only contribution were calculated according to reference.<sup>46</sup>

The AILFT matrix<sup>47</sup> was calculated using the ORCA 5.0.3 quantum chemistry package,<sup>48</sup> with SARC-DKH-DEF2-TZVP(-f) basis sets<sup>49,50</sup> and AUTOAUX feature<sup>51</sup> to automatically generate auxiliary basis sets for the resolution of identity approximation (RI-JK).<sup>52</sup> Scalar relativistic effects were accounted for using the second-order scalar relativistic Douglas Kroll Hess (DKH2) Hamiltonian formalism.<sup>53</sup> The CASSCF calculation was performed with a CAS(n,7), as for MOLCAS with

all states with  $S_{max}$  spin multiplicity. The CASSCF energies are very similar to those obtained with MOLCAS, and are not given.

The crystal field parameters (CFPs) were calculated using ITO decomposition.<sup>54</sup> i) the AILFT matrices (of size  $L = 3$ ) lead to the CFPs at orbital level, ii) the SF-CASSCF matrices (of size  $L$ ) provide CFPs including many-electrons effects, iii) the SO-CASSCF matrices (of size  $J$ ) provide the CFPs including spin-orbit coupling, either including only the states with  $S_{max}$  or with all spin-states. iv) Finally, the SO-CASPT2 matrices (of size  $J$ ) provide the CFPs including effectively many-electron, spin-orbit mixing and dynamical correlation effects.

**DFT Calculations.** Unrestricted DFT calculations were performed with ORCA version 5.0.3. Scalar relativistic effects were taken into account with ZORA Hamiltonian.<sup>55</sup> The ‘‘resolution of identity’’ RIJCOSX approximation was used for the formation of the Coulomb and exchange-type matrices.<sup>52</sup> The SARC-ZORA-TZVP basis set was used for An atoms with the SARC/J auxiliary basis set.<sup>56</sup> For a better description of the spin population near the nuclei, the IGLO-II basis set was used for the N and O atoms<sup>57</sup> with the auxiliary basis sets using the AUTOAUX feature. Comparisons with SARC-ZORA-TZVPP for the An atoms and IGLO-III, EPR-II<sup>58</sup> and aug-cc-pVTZ-J<sup>59</sup> for the N and O atoms were performed leading to similar results. The option DefGrid3 was used for the angular grid. Seven different functionals were considered, two nonhybrid PBE<sup>60</sup> and BLYP,<sup>7</sup> four hybrid PBE0,<sup>60</sup> B1LYP,<sup>61</sup> B3LYP<sup>62</sup> and BHLYP<sup>63</sup> and two range-separated hybrid functionals, LC-BLYP<sup>7</sup> and CAM-B3LYP.<sup>64</sup> The ligand hyperfine coupling (HFC) constants are deduced from the spin density at the position of the nuclei  $\rho(\mathbf{r}_K)$  according to Eq. 4 and averaged on chemically equivalent atoms. Spin Mullikens populations are calculated with MOLCAS using an average of configurations for the 5f orbitals.<sup>65</sup>

## Results and discussion

### Geometry of the complexes

X-rays structures of solid  $[(\text{C}_2\text{H}_5)_4\text{N}]_2\text{An}^{\text{IV}}(\text{NO}_3)_6$ <sup>22,66</sup> show that the oxygen atoms of the coordination sphere are at the corners of an irregular icosahedron. Due to the presence of the counter-ions, there are significant differences in the U–O distances. NMR experiments presented in this work are performed in solution and one expects all An–O distances to be identical in solution.<sup>22</sup> We therefore built symmetrized complexes from crystallographic structures spanning the  $\mathcal{T}_h$  group using ChemCraft

software<sup>67</sup> (see Table S1). The twelve coordinating oxygen atoms, denoted  $O_{\text{int}}$ , form a dodecahedron with pyritohedral symmetry (see Figure S1) and the six nitrogen atoms form an octahedron. The three two-fold axes join two opposite N atoms while the four three-fold axes point towards the center of triangles formed by three  $O_{\text{int}}$  atoms belonging to adjacent nitrate groups. The six non-coordinating O atoms are denoted  $O_{\text{ext}}$ .

## Electronic structure

The 5f orbitals of the  $[\text{U}^{\text{IV}}(\text{NO}_3)_6]^{2-}$  complex are depicted in Figure 1. They span the  $a_u \oplus 2t_u$  irreps. The lowest  $t_u$  and the  $a_u$  manifolds are mostly non-bonding. There are two  $f_{\pm 3}$  orbitals in the plane perpendicular to each  $C_3$  axis, one with the different lobes pointing in between two  $O_{\text{int}}$  atoms and non-bonding, the other one pointing towards the  $O_{\text{int}}$  atoms, and strongly anti-bonding. The  $f_{xyz}$  orbital spans the  $a_u$  irrep and the 8 lobes point in between the  $O_{\text{int}}$  atoms as well, it is only 500  $\text{cm}^{-1}$  above the non-bonding  $t_u$  manifold.

The energy levels of the three  $[\text{An}^{\text{IV}}(\text{NO}_3)_6]^{2-}$  complexes were calculated with CASSCF and CASPT2 methods (see Tables in Section S3.1). The results for the XRD structures are similar to the symmetrized ones, except the lifting of the degeneracy of the different manifolds. The splitting of the ground  $J$  manifold is between 1100 ( $\text{U}^{\text{IV}}$ ) and 2000 ( $\text{Pu}^{\text{IV}}$ )  $\text{cm}^{-1}$ . This is larger than for the  $\text{An}^{\text{IV}}$ -DPA (1100 - 1500  $\text{cm}^{-1}$ ) and the aquo  $\text{An}^{\text{IV}}$  (700 - 1200  $\text{cm}^{-1}$ ) series. The ground state is degenerate for the three complexes, threefold  $T_g$  for the  $\text{U}^{\text{IV}}$  and  $\text{Pu}^{\text{IV}}$  and fourfold  $F_{3/2,u}$  for  $[\text{Np}^{\text{IV}}(\text{NO}_3)_6]^{2-}$  (cf Table S5). Those states have an isotropic magnetic moment, with opposite orbital and spin contributions, as expected from third Hund's rule.

CFPs and strength parameters were calculated, with  $z$  along one of the  $C_3$  axis (see Tables in Section S3.2). As expected from the  $\mathcal{T}_h$  symmetry, only the axial CFPs  $B_0^2$ ,  $B_0^4$ ,  $B_0^6$  and the ternary  $B_3^4$ ,  $B_3^6$  and  $B_6^6$  do not vanish. Crystal field theory models the interaction of the active 5f electrons with the ligands. Originally issued from the expansion of the electrostatic interaction, the CFPs effectively describe other interactions. The crystal field model Hamiltonian is a one-electron operator, the electron-electron interaction and spin-orbit coupling being described by their own parameters,  $F^k$  and  $\zeta$ , respectively. The CFPs at this level are provided by the AILFT, developed by Atanasov.<sup>69</sup> The ITO technique proposed by Ungur and Chibotaru<sup>54</sup> allows the calculation of the CFPs from the many-electron wave-functions, with or without spin-orbit, with or without dynamical correlation.<sup>70</sup> In one word, with the CFPs deduced from SO-CASPT2 for example, one can calculate the  $2J + 1$  energies and wave-functions of the ground  $J$  manifold.

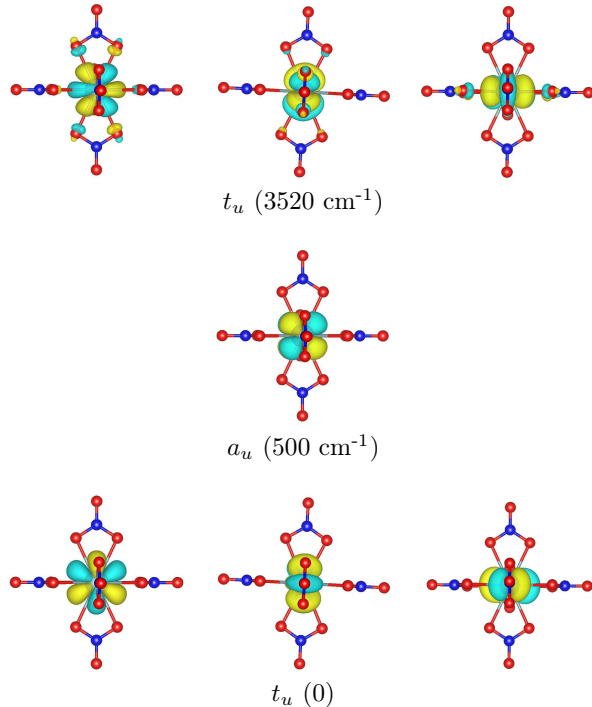


**Figure 1:** 5f active orbitals of  $[\text{U}^{\text{IV}}(\text{NO}_3)_6]^{2-}$ . Orbitals are labeled according to  $\mathcal{T}_h$  irreps. The energies are given in  $\text{cm}^{-1}$ . The isovalue is 0.025 e/bohr<sup>3</sup>.

The CFPs can be summed up to the crystal field strength parameter  $S$  which is rotation invariant and allows an easy comparison between complexes (see Figure 2). In the  $[\text{An}^{\text{IV}}(\text{NO}_3)_6]^{2-}$  series,  $S$  ranges in the 1000 - 2000  $\text{cm}^{-1}$  window, larger than for the  $\text{An}^{\text{IV}}$ -DPA series. At orbital level,  $S$  decreases from 2000 to 1500  $\text{cm}^{-1}$ .  $B_0^2$  is zero due to the cubic symmetry and the 6th order is largely dominant. CFPs from SF-CASSCF are similar to the orbital ones for  $[\text{Np}^{\text{IV}}(\text{NO}_3)_6]^{2-}$  and  $[\text{Pu}^{\text{IV}}(\text{NO}_3)_6]^{2-}$  but differ for  $[\text{U}^{\text{IV}}(\text{NO}_3)_6]^{2-}$ . This is confirmed by the larger distance between the model and ab initio matrices (see Table S8) and it shows that the many-electron wave function departs from the free-ion with  $L = 5$ . The introduction of spin-orbit coupling affects the CFPs, as usually for actinides. It leads to a larger effective crystal field for the  $\text{Pu}^{\text{IV}}$  complex, with an important increase of the 2nd and 4th orders. The dynamical correlation does not affect so much. Finally, the SO-CASPT2 CFPs increase in the series, contrarily to the orbital one, mostly due to the effects of spin-orbit.

## Magnetic susceptibility

The magnetic susceptibilities evaluated with Evans method are given in Table 1 and compared to the SO-CASPT2 values. The agreement is good, with a slight underestimation and overestimation for  $\text{U}^{\text{IV}}$  and  $\text{Pu}^{\text{IV}}$ , respectively (Figure 3). The SO-CASPT2 values obtained for the XRD structures are very similar.  $\chi$  in the  $[\text{An}^{\text{IV}}(\text{NO}_3)_6]^{2-}$  series

**Table 1:** Total  $\chi$  and spin-only  $\chi^S$  magnetic susceptibilities (in  $10^{-8} \text{ m}^3 \cdot \text{mol}^{-1}$ ) of  $[\text{An}^{\text{IV}}(\text{NO}_3)_6]^{2-}$  complexes at 298 K from Evans method (exp) and ab initio calculations.

	$\text{U}^{\text{IV}}$		$\text{Np}^{\text{IV}}$		$\text{Pu}^{\text{IV}}$	
	$\chi$	$\chi^S$	$\chi$	$\chi^S$	$\chi$	$\chi^S$
SO-CASSCF	3.85	-2.24	3.91	-3.14	1.43	-2.24
SO-CASPT2	3.27	-2.02	3.87	-3.06	1.29	-2.16
exp	3.64 ( $\pm 0.09$ )		3.84 ( $\pm 0.11$ )		0.90 ( $\pm 0.14$ )	
LS coupling <sup>a</sup>	6.70	-3.36	6.87	-5.14	3.77	-5.02

<sup>a</sup> :  $\chi_{LS} = \kappa \frac{g_J^2 J(J+1)}{3T}$  and  $\chi_{LS}^S = \kappa \frac{-S J g_e g_J}{3T}$  with  $\kappa = \frac{N_A \mu_0 \mu_B^2}{k}$ , see Section S4.2

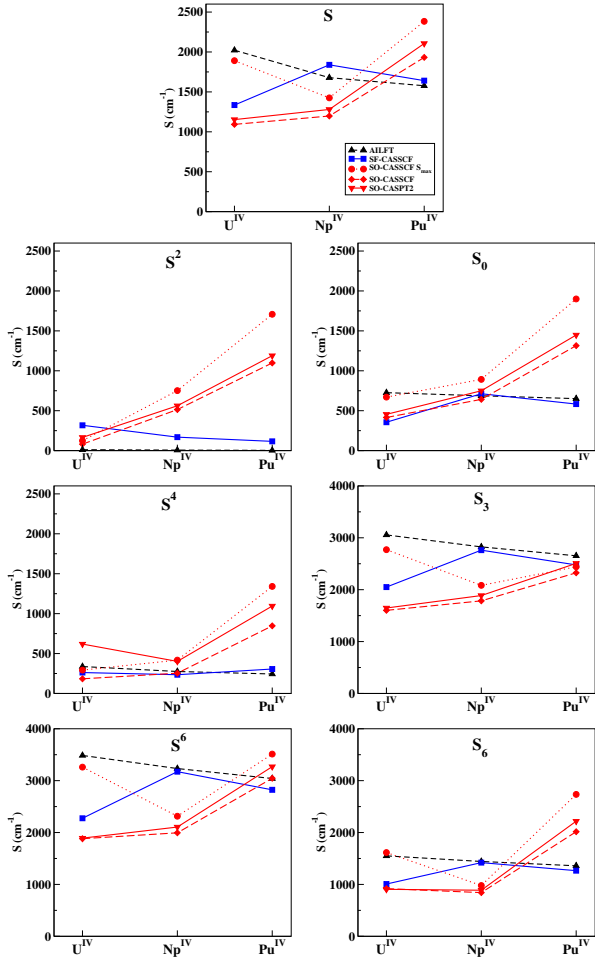


**Figure 2:** Crystal field strength parameters (in  $\text{cm}^{-1}$ ) in the  $[\text{An}^{\text{IV}}(\text{NO}_3)_6]^{2-}$  series. black: orbital level (AILFT), blue:  $L$  level (SF-CASSCF), red:  $J$  level (SO-CASSCF  $S_{max}$ , SO-CASSCF and SO-CASPT2).

is strongly reduced from the LS coupling scheme value, which is observed for the isoelectronic lanthanides. It has been shown<sup>27,71</sup> that this reduction arises i) from the large splitting of the ground  $J$  manifold, much larger than the thermal room temperature energy. The contribution of the most destabilized  $J$  components do not contribute to  $\chi$ . ii) The  $J$ -mixing with excited  $J$ -manifolds tends to reduce  $\chi$ . The reduction from the LS value is about 50 % in the  $[\text{An}^{\text{IV}}(\text{NO}_3)_6]^{2-}$  series, and even larger for the aquo and DPA complexes (about 70 %<sup>14,68</sup>). It is in accordance with the crystal field strength parameter twice larger in the present series than in the DPA one. In the aquo and DPA complexes, the coordination number is 8 and 9 with An-O distances in the 2.35 - 2.41 Å range. The  $\text{AnO}_{12}$  coordination sphere is more compact even if the An-O distances are slightly larger by 0.1 Å. Thus, the reduction of  $\chi$  compared to the previous series is due to the larger coordination number, and follows the large increase of the crystal field strength parameter  $S$  and the even larger reduction for the  $\text{Pu}^{\text{IV}}$  arises from a larger  $J$ -mixing.<sup>72,73</sup>

The temperature dependence of both the Evans and SO-CASPT2 curves denote a  $1/T$  behavior in accordance with Curie law (see Figures S4 and S6).

## <sup>15</sup>N and <sup>17</sup>O NMR spectroscopy

<sup>15</sup>N and <sup>17</sup>O NMR spectra of  $[\text{An}^{\text{IV}}(\text{NO}_3)_6]^{2-}$  complexes were recorded in  $\text{CD}_3\text{CN}$  at different temperatures from 223 to 325 K (Figure 4 as an example and Figures S7, S8 and Tables S11, S13 for details). <sup>15</sup>N resonance of the acetonitrile diluent is used as reference and set at -133.5 ppm all along the temperature range. The absence of free nitrates that may arise from nitric acid or TEA nitrate excess was checked by looking for <sup>15</sup>N signal around 0 ppm (Figure 5): All  $[\text{An}^{\text{IV}}(\text{NO}_3)_6]^{2-}$  samples present only one <sup>15</sup>N signal that belongs to the nitrates surrounding the  $\text{An}^{\text{IV}}$  cations. The amount of water in deuterated acetonitrile is determined from <sup>1</sup>H spectra and found to be around 0.03 mol.L<sup>-1</sup> for Th to Pu. This amount is maintained as low as possible in order to avoid water/nitrate competition in the first coordination sphere of  $\text{An}^{\text{IV}}$ . On the other hand,

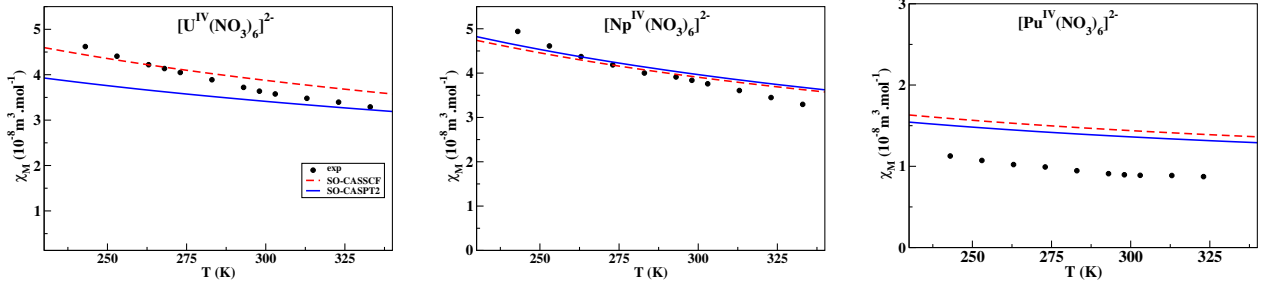


**Figure 3:** Experimental and calculated (SO-CASSCF and SO-CASPT2) magnetic susceptibility  $\chi$  with temperature (in K) of the  $[\text{An}^{\text{IV}}(\text{NO}_3)_6]^{2-}$  complexes.

this small amount of water is required as reference scale (set at 0 ppm) in  $^{17}\text{O}$  NMR spectra. Despite these optimized experimental conditions, we looked for chemical exchange effects accountable for chemical shift variations with temperature. In order to study temperature dependency only arising from paramagnetic shifts we sought to uncorrelate the effects due to chemical exchange from those of paramagnetic shifts (see Section S5.1 for details).

The signals of the two different  $^{17}\text{O}$  sites can be distinguished at room temperature for the  $[\text{U}^{\text{IV}}(\text{NO}_3)_6]^{2-}$  complex (see Figure 5), with signals at 529 and 430 ppm, for  $\text{O}_{\text{int}}$  and  $\text{O}_{\text{ext}}$  respectively. For the  $\text{Th}^{\text{IV}}$ ,  $\text{Np}^{\text{IV}}$  and  $\text{Pu}^{\text{IV}}$  complexes, the  $\text{O}_{\text{int}}$  peak appears at 427, 442 and 429 ppm respectively and probably overlaps the signal of  $\text{O}_{\text{ext}}$  since the  $\text{O}_{\text{int}}$  peak line width is at least 1000 Hz large ( $\approx 20$  ppm). Nitrate anions may undergo a fast three-fold jumps at room temperature as observed in  $\text{NaNO}_3$  solid state.<sup>74</sup> Hung et al. determined an exchange constant rate of about  $10^7$  Hz at room temperature by simulating  $^{17}\text{O}$  solid state NMR spectra.<sup>75</sup> It has to be mentioned that nitrates in the  $\text{NaNO}_3$  sample are monodentate and present crystallographically equivalent oxygens linked to two sodium atoms.<sup>76</sup> Conversely, nitrates of  $[\text{An}^{\text{IV}}(\text{NO}_3)_6]^{2-}$  complexes are in bidentate chelating mode and assumed to adopt a more stable conformation. A  $^{15}\text{N}$  and  $^{17}\text{O}$  line width analysis (see S5.1 in SI) allow to eliminate the hypothesis of fast chemical exchange in nitrates. Consequently, we considered thereafter a simple signal overlapping of  $\text{O}_{\text{ext}}/\text{O}_{\text{int}}$  sites.

***pNMR shifts*** The presence of a paramagnetic center induces an additional shift  $\delta_K^p$  for a ligand atom  $K$  with respect to a diamagnetic analog.  $[\text{Th}^{\text{IV}}(\text{NO}_3)_6]^{2-}$  was used as diamagnetic reference at 235 K. The Actinide Induced Shift (AIS)  $\delta_K^p$  can be separated in pseudocontact or dipolar  $\delta_K^{pc}$  and Fermi contact  $\delta_K^c$  components

$$\delta_K^p = \delta_K^{pc} + \delta_K^c \quad (2)$$

$\delta_K^c$  depends on the electron spin density of the paramagnetic cation delocalized and/or polarized onto

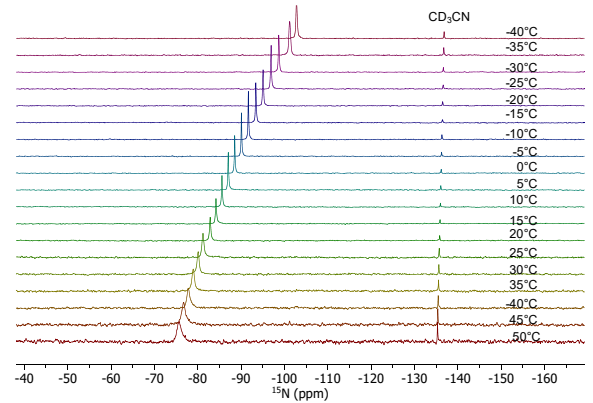


**Figure 4:**  $^{15}\text{N}$  NMR spectra of  $[\text{Pu}^{\text{IV}}(\text{NO}_3)_6]^{2-}$  complex in  $\text{CD}_3\text{CN}$  solution from 235 to 314K.  $^{15}\text{N}$  signal of  $\text{CD}_3\text{CN}$  is used as reference at 133.5 ppm.

the  $K$  nucleus. It can be expressed as<sup>73</sup>

$$\delta_K^c = \frac{1}{\mu_0 \hbar \mu_B g_e \gamma_K N_A} A_K^c \chi^S \quad (3)$$

where  $\gamma_K$  is the gyromagnetic ratio of the observed nuclei ( $\gamma^{15\text{N}} = -4.316$  MHz/T and  $\gamma^{17\text{O}} = -5.774$  MHz/T),  $A_K^c$  the HFC constant and  $\chi^S$  the spin contribution to the magnetic susceptibility.  $N_A$  is the Avogadro constant,  $\mu_0$  the magnetic permeability,  $\mu_B$  the Bohr magneton and  $g_e$  is the free electron  $g$ -factor.

The pseudocontact shift  $\delta_K^{pc}$  corresponds to the through-space magnetic dipolar interaction between the electronic magnetic moment of the paramagnetic center and the  $K$  nuclear magnetic moment, in the point-dipole approximation.<sup>77</sup>  $\delta_K^{pc}$  depends on the anisotropy of the magnetic susceptibility tensor  $\chi$ .<sup>78</sup> As discussed in the previous Section, the magnetic susceptibility is isotropic in the  $[\text{An}^{\text{IV}}(\text{NO}_3)_6]^{2-}$  series due to the cubic symmetry, and the dipolar contribution to the AIS is zero. This contrasts with  $^{15}\text{N}$  NMR of mononitrato complexes of lanthanide performed at very low temperature ( $-95$  °C) in water-acetone mixture.<sup>79,80</sup> With one nitrate in coordination sphere completed by water molecules, we can expect a non symmetric conformation and thus paramagnetic chemical shifts mainly driven by dipolar interactions.

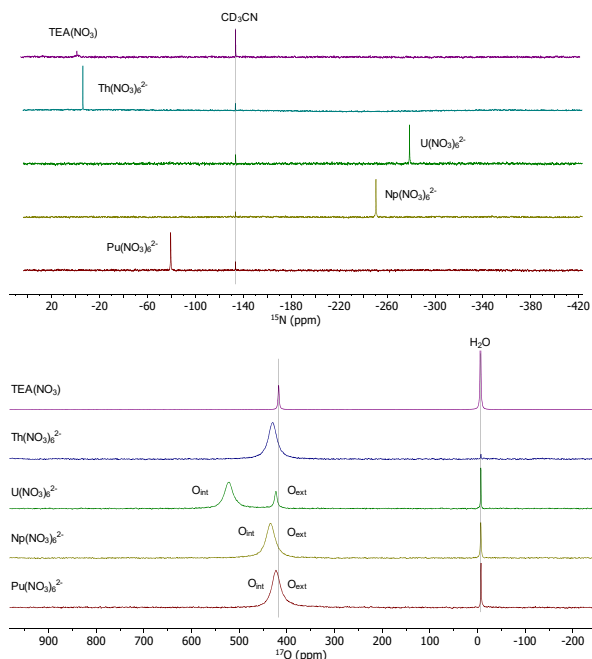


**Figure 5:**  $^{15}\text{N}$  (top) and  $^{17}\text{O}$  (bottom) NMR spectra of  $[\text{An}^{\text{IV}}(\text{NO}_3)_6]^{2-} \cdot 2[(\text{C}_2\text{H}_5)_4\text{N}]^+$  complexes in  $\text{CD}_3\text{CN}$  solution recorded at 298 K.  $^{15}\text{N}$  scale is set to  $\text{CH}_3\text{CN}$  shift at  $-133.5$  ppm (in  $^{15}\text{N}$  reference scale to  $\text{CH}_3\text{NO}_2$ ) and  $^{17}\text{O}$  scale is set to water at 0 ppm. Spectrum of the TEA nitrate is given for comparison on the top.

The  $^{15}\text{N}$  and  $^{17}\text{O}$  AIS are reported in Tables S12 and S14 respectively and the temperature-dependent chemical shifts are shown in Figures 6, S7, S8 and in Tables S11 and S13. The AIS for the  $^{15}\text{N}$  and the  $^{17}\text{O}$  of  $\text{O}_{\text{int}}$  of the  $\text{U}^{\text{IV}}$  complex have a pure  $T^{-1}$  behavior. This is in agreement with Golding findings for the contact term of isotropic compounds<sup>81</sup> and with our previous study of  $\text{An}^{\text{IV}}$ -DPA complexes.<sup>14</sup> The SO-CASPT2  $\chi^S$  curves denote the same pure  $T^{-1}$  behavior (see Figure S6). It follows from Eq. 3 that the HFC constant  $A_K^c$  is temperature-independent. The values for the other  $^{17}\text{O}$  signals are small and their temperature dependence is less clear.

For  $[\text{U}^{\text{IV}}(\text{NO}_3)_6]^{2-}$ , the  $\text{O}_{\text{ext}}$  signal seems to behave independently with temperature like  $^{17}\text{O}$  signals of  $[\text{Np}^{\text{IV}}(\text{NO}_3)_6]^{2-}$  and  $[\text{Pu}^{\text{IV}}(\text{NO}_3)_6]^{2-}$  compounds. An increasing dispersion of data is observed while lowering temperature and could be explained by i) line broadening due to the quadrupolar  $^{17}\text{O}$  nucleus with the media viscosity and ii) the shouldering of  $\text{O}_{\text{int}}$  and  $\text{O}_{\text{ext}}$  signal making the peak picking difficult to determine in the case of the  $[\text{Np}^{\text{IV}}(\text{NO}_3)_6]^{2-}$  and  $[\text{Pu}^{\text{IV}}(\text{NO}_3)_6]^{2-}$  compounds.

pNMR shifts can be evaluated from first principles based on the formula derived by Kurland and McGarvey.<sup>82-84</sup> It has been successfully applied with CAS based methods to lanthanide and actinide complexes, where the dipolar term is dominant.<sup>31, 85-88</sup> This approach turns out to be more

limited for cases where the Fermi contact contribution is important. In this work, the AIS are calculated using Eq. 3.<sup>14</sup> To do this, one needs the value of  $\chi^S$  which depends on the paramagnetic center only and is well described by CAS based methods and the ligands HFC constant which needs a good description of the spin delocalization and polarization which is correctly described by unrestricted DFT methods.  $\chi^S$  calculated with SO-CASSCF and SO-CASPT2 are given in Table 1. As for the total  $\chi$ ,  $\chi^S$  is strongly reduced compared to the LS coupling scheme values calculated in Section S4.2, and is reduced compared to the DPA complexes. It shows again that the strength of the crystal field makes the use of the tabulated values of  $\langle S_z \rangle$  for lanthanides inappropriate for actinides.<sup>26, 89, 90</sup>  $\chi^S$  is larger for  $\text{Np}^{\text{IV}}$  and  $\text{Pu}^{\text{IV}}$  due to their larger spin value  $S$  but slightly decrease for  $\text{Pu}^{\text{IV}}$  due to the decrease of  $g_J$ . The HFC constants were calculated for the  $^{15}\text{N}$  and  $^{17}\text{O}$  nuclei, using unrestricted DFT with different functionals (see Tables 3 and S17).

The AIS calculated with the two CAS methods and three types of functionals are compared in Table 2. In all cases, the signs and the trends are the same. The functional affects strongly the HFC constant as will be discussed in details in the next Section. The calculated values are in the right range compared to the experimental ones, but it is not always the same functional that fits best. Surprisingly, the calculations predict two well distinct AIS for  $\text{O}_{\text{int}}$  and  $\text{O}_{\text{ext}}$  in the three complexes, the largest gap being for  $[\text{Pu}^{\text{IV}}(\text{NO}_3)_6]^{2-}$  while experimentally only  $\text{U}^{\text{IV}}$  presents two distinct signals. It has to be mentioned that  $^{17}\text{O}$  spectra suffer from low resolution since peak line width are at least 1000 Hz ( $> 20$  ppm see Table S13) large in the best case. Would the  $\text{O}_{\text{int}}$  and  $\text{O}_{\text{ext}}$  signals be less separated than predicted by the calculation (about 130 ppm), an experimental overlap of both signals could be observed. However, the discrepancy between experimental and calculated  $^{15}\text{N}$  AIS arises from computed values since experimental resolution for half integer spins is excellent ( $\approx 20$  Hz, see Table S11).

**HFC constants** Experimental values for the HFC constant can be evaluated from Eq. 3. As discussed previously, for actinide complexes,  $\chi^S$  depends on the ligand environment, contrarily to the lanthanides where  $\chi^S$  can be taken as its free ion value. To evaluate an experimental value for the HFC constants, one needs consequently to use the SO-CASPT2  $\chi^S$ . They are compared to the DFT values in Tables 3 and S17. Our calculations are performed at the scalar relativistic level for practical reasons. It has been shown that the spin-orbit coupling can play a preponderant role, even changing the sign.<sup>91</sup> The trends are the same for the three complexes, and for all functionals:  $A_{\text{O}_{\text{int}}}$  is positive in the range 0.4;1.3,  $A_{\text{N}}$  is negative, and

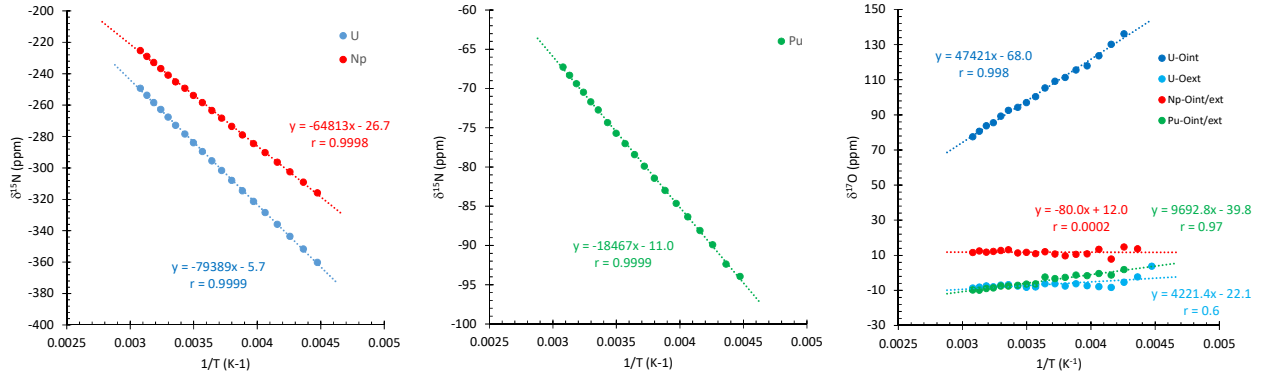


**Figure 6:** AIS (in ppm) vs  $T^{-1}$  (in  $K^{-1}$ ) in the 233 - 323 K temperature range. Left:  $^{15}\text{N}$  for  $\text{U}^{\text{IV}}$  and  $\text{Np}^{\text{IV}}$ , middle:  $^{15}\text{N}$  for  $\text{Pu}^{\text{IV}}$ , right:  $^{17}\text{O}$  for  $\text{U}^{\text{IV}}$ ,  $\text{Np}^{\text{IV}}$  and  $\text{Pu}^{\text{IV}}$ . Linear regressions are represented in dashed lines.

**Table 2:** AIS (in ppm) at 300 K calculated from Eq. 3 with  $\chi^S$  calculated with SO-CASSCF or SO-CASPT2 and  $A_K^c$  deduced from DFT with three different functionals. The experimental values are given for comparison (from Tables S12 and S14)

	$\delta_{\text{O}_{\text{int}}}^{\text{P}}$		$\delta_{\text{N}}^{\text{P}}$		$\delta_{\text{O}_{\text{ext}}}^{\text{P}}$	
	SO-CASSCF	SO-CASPT2	SO-CASSCF	SO-CASPT2	SO-CASSCF	SO-CASPT2
	$[\text{U}^{\text{IV}}(\text{NO}_3)_6]^{2-}$					
BLYP	37.2	34.1	-348.3	-319.9	-7.1	-6.5
B3LYP	99.3	91.2	-236.5	-217.3	-9.4	-8.6
CAM-B3LYP	126.8	116.4	-197.7	-181.6	-6.2	-5.7
exp	92.6		-272.8		-6.7	
	$[\text{Np}^{\text{IV}}(\text{NO}_3)_6]^{2-}$					
BLYP	30.4	29.5	-349.7	-339.7	0.7	0.7
B3LYP	100.5	97.6	-247.8	-240.7	-8.1	-7.9
CAM-B3LYP	133.4	129.6	-217.4	-211.1	-5.5	-5.3
exp			-245.2		13.2	
	$[\text{Pu}^{\text{IV}}(\text{NO}_3)_6]^{2-}$					
BLYP	59.0	56.9	-164.8	-158.8	9.9	9.5
B3LYP	120.4	116.0	-119.1	-114.8	2.9	2.8
CAM-B3LYP	146.1	140.8	-103.1	-99.4	1.8	1.8
exp			-72.7		-7.5	

**Table 3:**  $^{15}\text{N}$  and  $^{17}\text{O}$  HFC constants (in MHz), deduced from AIS using SO-CASPT2  $\chi^S$  values at 298 K with Eq. 3 (denoted **exp**) and calculated with UDFT.

$A_K$	$\text{U}^{\text{IV}}$				$\text{Np}^{\text{IV}}$				$\text{Pu}^{\text{IV}}$			
	exp	BLYP	B3LYP	CAM-B3LYP	exp	BLYP	B3LYP	CAM-B3LYP	exp	BLYP	B3LYP	CAM-B3LYP
$\text{O}_{\text{int}}$	0.36	0.27	0.72	0.912	0.16	0.52	0.69		0.43	0.87	1.06	
N	-0.80	-1.89	-1.28	-1.07	-0.72	-1.35	-0.96	-0.84	-0.21	-0.89	-0.64	-0.56
$\text{O}_{\text{ext}}$	-0.03	-0.05	-0.07	-0.04	0.05	0.00	-0.04	-0.03	-0.03	0.07	0.02	0.01

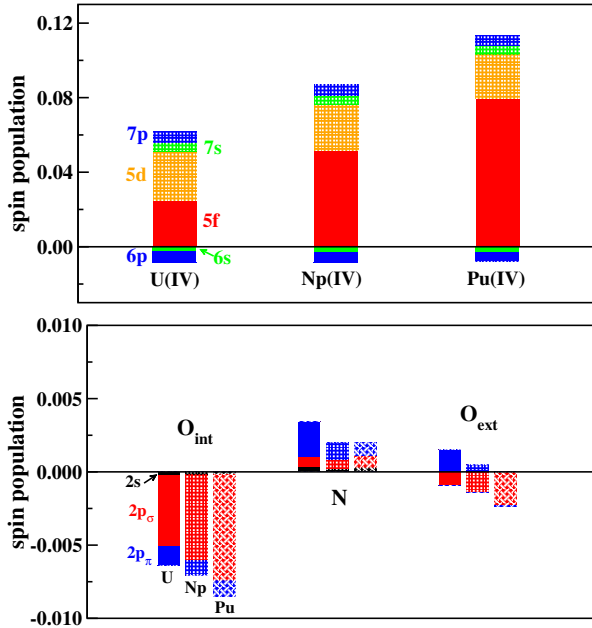


**Figure 7:** Contributions from AOs to Mulliken spin population  $(\rho_{BPED0} - \rho_{CAS})/N$  where  $N$  is the number of unpaired  $f$  electrons. (up) for the metal; (down) for the ligands atoms.

larger in magnitude, in the range -2.0;-0.4 and  $A_{O_{ext}}$  is much smaller, positive or negative according to the functional, in the range -0.1;0.1. Since the gyromagnetic ratios  $\gamma_{15N}$  and  $\gamma_{17O}$  are of the same sign, the change of sign between  $O_{int}$  and N denotes a spin polarization mechanism. The trends in the series are the same with all functionals:  $A_N$  is divided by a factor 2 from  $U^{IV}$  to  $Pu^{IV}$ , while  $A_{O_{int}}$  decreases between  $U^{IV}$  and  $Np^{IV}$  and increases for  $Pu^{IV}$  to become larger than for  $U^{IV}$ . The trends are the same for the available experimental values, with a much larger decrease for  $A_N$  between  $Np^{IV}$  and  $Pu^{IV}$ . With the increase of the amount of Hartree-Fock exchange in the functional,  $A_{O_{int}}$  increases and  $|A_N|$  decreases, denoting a change of the balance of the spin density on the ligands. For  $A_N$ , the best fit to experimental values is reached by increasing the Hartree-Fock exchange while the fit to the only available experimental  $A_{O_{int}}$  value is obtained with the GGA functionals.

The Mulliken populations are analyzed in details in Section S5.4 and are shown in Figure 7. The spin density is mostly borne by the  $5f$  orbitals and the polarization plays the key role over the delocalization. The unpaired spins can polarize the paired spins in lower lying orbitals.<sup>90</sup> The main contributions in the metallic orbitals are in the  $6d$  due to the sole polarization and in the occupied  $6p$  where delocalization and polarization cancels partly each other.

In the non relativistic limit,  $A_K^c$  can be expressed in terms of the spin density at the position of the

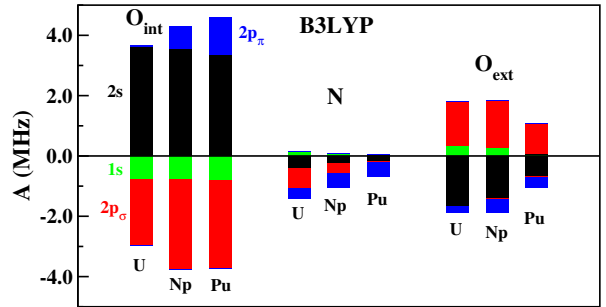


**Figure 8:** Contributions from ligands atomic orbitals to  $A_K^c$  (in MHz) calculated with B3LYP.

nucleus  $K$   $\rho^S(\mathbf{r}_K)^{24,92,93}$

$$A_K^c = \frac{\mu_0 \mu_B g_e \gamma_K \hbar}{3S} \rho^S(\mathbf{r}_K) \quad (4)$$

where  $S$  is the spin.  $A_K^c$  can subsequently be decomposed in MOs contributions as given in Table S18 and shown in Figure S11. The ligand MOs are shown in Figure S3. The MO decomposition has been very informative for the analysis of ligand HFC constants in transition metal complexes.<sup>94-97</sup> For  $O_{int}$  and  $O_{ext}$ , the largest contribution arises from the  $6p$  of the metal which is negative, counterbalanced by a large positive contribution from the  $2\sigma_{2s}^b$  block. The  $2\sigma_{2s}^b$  orbital is developed on the three oxygen atoms, but denotes a node on the central nitrogen atom, so the  $6p-2\sigma_{2s}^b$  interaction does not bring spin density on those atoms. It shows that the ligands MOs contributing to  $A_K^c$  are those in bonding interaction with a metallic AO bearing spin density. But the bonding and anti-bonding orbitals contribute with opposite signs, so it is the sum of that should be analyzed.

The ligands MOs issued from the  $2s$  interact with the metallic  $6p$ , while those built from the  $2p$  interact with the occupied  $5f$  and vacant  $6d$  orbitals. In order to gain in readability, the contributions are grouped by type of AO, by summing over large contributions of opposite sign. We take further advantage of the planar symmetry of the ligands, separating the  $\sigma$  and  $\pi$  contributions. Since the metallic  $6p$  interacts with the different  $\sigma_{2s}$  MOs, its contribution was included in the  $2s$  group. The AOs contributions to  $A_K^c$  are shown in Figure 8 for B3LYP (and in Figure S12 for BLYP and CAM-B3LYP). The  $2s$  orbitals bring the largest contributions for the two types of oxygen atoms, with opposite signs, positive for  $O_{int}$ , negative and smaller for  $O_{ext}$ . This emphasizes the importance of the interaction with the metallic  $6p$  orbitals. The  $2p_\sigma$  contribution is almost as large, and actually larger for N: its sign is alternating as well, opposite to the the  $2s$  contribution for the oxygen atoms, but not for N. The  $2p_\pi$  contribution is smaller,  $\pi$  bonding being less efficient than  $\sigma$  one. Its sign varies with the functional, depending on the relative energy with the  $5f$  orbitals. Since the  $2p$  and  $2s$  contributions

are opposite in sign for the oxygen atoms, there is a partial cancellation, while they are additive for the nitrogen atoms. Finally,  $A_K^c$  is the largest for N, even the different contributions are smaller, opposite to  $O_{\text{int}}$  due to the large positive  $2s$  contribution, and evanescent for  $O_{\text{ext}}$  due to the cancellation of  $2s$  and  $2p$  contributions. For all atoms,  $1s$  and  $2s$  contributions are opposite in sign.<sup>98,99</sup> It becomes clear why HFC constants varies so much with the functional, and more precisely with the amount of Hartree-Fock exchange which impacts the balance between the different bonding modes. The effect of the amount of exact exchange on ligands HFC constants has been analyzed in transition metal complexes and hybrid functionals are often those fitting the best experimental values<sup>94,100–102</sup>

This analysis highlights two pathways between the spin density borne by the  $5f$  orbitals and the nuclei of the ligand: i) the direct interaction between the  $5f$  and the  $2p$  ligand MOs, with a participation of the  $6d$  ii) the spin polarization of the metallic  $6p$  orbitals (see Section S5.4) which interact with the  $2s$  of the ligands.

By comparing the three complexes, we observe that overall all the AO contributions decrease in the series with the exception of  $2p$  contributions to the  $O_{\text{int}}$  atoms. This was not clear from the MO contributions, where the bonding the  $6p_{\text{An}} - 2\sigma_{2s}^b$  interaction increases from  $\text{U}^{\text{IV}}$  to  $\text{Pu}^{\text{IV}}$  following the smaller energy gap between the two interacting orbitals. The overall decrease is consistent with an overall decrease of the metal-ligand bonding interactions.

## Conclusion

Magnetic susceptibility has been evaluated using Evans method for  $[\text{An}^{\text{IV}}(\text{NO}_3)_6]^{2-}$  complexes dissolved in  $\text{CD}_3\text{CN}$  solution which maintains the first coordination sphere as demonstrated from UV-vis spectra. For SO-CASPT2 calculations, the symmetrized structures in the cubic  $T_h$  group are considered. The magnetic susceptibility tensor is isotropic with values in good agreement with the Evans values. The CFPs are deduced from the ab initio calculations, either at the orbital level, or including effectively the different interactions. The crystal field strength parameter  $S$  is about  $3000\text{ cm}^{-1}$ , denoting an important metal-ligand interaction, in accordance with the large coordination number.  $S$  decreases from  $\text{U}^{\text{IV}}$  to  $\text{Pu}^{\text{IV}}$  at the orbital level and increases otherwise. This confirms that for actinide complexes, the J-mixing affects quantitatively the CFPs when describing the ground J-manifold.

$^{15}\text{N}$  and  $^{17}\text{O}$  paramagnetic chemical shifts were measured in the series. While the signals for the

two different  $^{17}\text{O}$  positions are well separated for the  $\text{U}^{\text{IV}}$  complex, they are not distinguishable for the  $\text{Np}^{\text{IV}}$  and  $\text{Pu}^{\text{IV}}$  complexes. Due to the cubic symmetry, the dipolar contribution to paramagnetic NMR shifts is quenched and the AIS result from pure contact interactions. This is consistent with the observed  $T^{-1}$  temperature-behavior. The AIS are calculated based on a SO-CASPT2/UDFT strategy, which gives a reasonable accordance with the experimental data and similar trends but predicts two well separated signals for the two  $^{17}\text{O}$  positions in the three complexes.

The ligands HFC constants calculated with different functionals or deduced from the experimental AIS show an alternation of sign between the bonding oxygen atom  $O_{\text{int}}$  and N, and a vanishing value for the external  $O_{\text{ext}}$ . Based on AO contributions to the HFC constants, it is shown that the sign alternation arises from the ligands  $2s$  orbitals, which get spin density through the bonding interaction with the metallic  $6p$  orbital, which itself is spin-polarized by the open-shell  $5f$  orbitals. The importance of the N HFC is due to the cumulative contributions of the  $2s$  and  $2p$  orbitals, with all the same sign, even if the contributions are all smaller. The  $2p$  ligands orbitals interact with the valence metallic  $5f$  hybridized with the more outer shell  $6d$  orbitals.

Thanks to the simple molecular structure and its high symmetry, we were able to deeply analyzed the AIS and the ligands HFC constants in the  $[\text{An}^{\text{IV}}(\text{NO}_3)_6]^{2-}$  complexes. And this shows that the signs and magnitude are difficult to foresee, since they arise from the interference of different pathways, sometimes additive, sometimes destructive.

## References

- [1] Neidig, M. L.; Clark, D. L.; Martin, R. L. Covalency in f-element complexes. *Coord. Chem. Rev.* **2013**, *257*, 394 – 406.
- [2] Choppin, G. R. Covalency in f-element bonds. *J. Alloys Compd.* **2002**, *344*, 55–59.
- [3] Choppin, G. R.; Jensen, M. P. Actinides in solution: complexation and kinetics. In *The chemistry of the actinide and transactinide elements*; Morss, L.; Edelstein, N.; Fuger, J., Eds.; Springer: Netherlands, 2006.
- [4] Gaunt, A. J.; Reilly, S. D.; Enriquez, A. E.; Scott, B. L.; Ibers, J. A.; Sekar, P.; Ingram, K. I. M.; Kaltsoyannis, N.; Neu, M. P. Experimental and Theoretical Comparison of Actinide and Lanthanide Bonding in  $\text{M}[\text{N}(\text{EPR}2)_2]_3$  Complexes (M = U, Pu, La, Ce; E = S, Se, Te; R = Ph, iPr, H). *Inorg. Chem.* **2008**, *47*, 29–41.
- [5] Roger, M.; Belkhir, L.; Arliguie, T.; Thuéry, P.; Boucekkine, A.; Ephritikhine, M. Uranium and Lanthanide Complexes with the 2-Mercapto Benzothiazolate Ligand: Evidence for a Specific Covalent Binding Site in the Differentiation of Isostructural Lanthanide(III) and Actinide(III) Compounds. *Organometallics* **2008**, *27*, 33–42.

- [6] Kaltsoyannis, N. Does covalency increase or decrease across the actinide series? Implications for minor actinide partitioning. *Inorg. Chem.* **2013**, *52*, 3407–3413.
- [7] Kelley, M. P.; Su, J.; Urban, M.; Luckey, M.; Batista, E. R.; Yang, P.; Shafer, J. C. On the origin of covalent bonding in heavy actinides. *Journal of the American Chemical Society* **2017**, *139*, 9901–9908.
- [8] Jung, J.; Atanasov, M.; Neese, F. Ab Initio ligand-field theory analysis and covalency trends in actinide and lanthanide free ions and octahedral complexes. *Inorg. Chem.* **2017**, *56*, 8802–8816.
- [9] Brennan, J. G.; Green, J. C.; Redfern, C. M. Covalency in bis([8]annulene)uranium from photoelectron spectroscopy with variable photon energy. *J. Am. Chem. Soc.* **1989**, *111*, 2373–2377.
- [10] Bursten, B. E.; Strittmatter, R. J. Cyclopentadienyl-Actinide Complexes: Bonding and Electronic Structure. *Angew. Chem. Int. Ed.* **1991**, *30*, 1069–1085.
- [11] Bursten, B. E.; Strittmatter, R. J. Characterization of Actinide Bonding in  $\text{Th}(\text{S}_2\text{PMe}_2)_4$  by Synchrotron X-ray Diffraction. *Inorg. Chem.* **1998**, *37*, 4559–4566.
- [12] Prodan, I. D.; Scuseria, G. E.; Martin, R. L. Covalency in the actinide dioxides: Systematic study of the electronic properties using screened hybrid density functional theory. *Phys. Rev. B: Condens. Matter* **2007**, *76*, 033101.
- [13] Kozimor, S. A.; Yang, P.; Batista, E. R.; Boland, K. S.; Burns, C. J.; Clark, D. L.; Conradson, S. D.; Martin, R. L.; Wilkerson, M. P.; Wolfsberg, L. E. Trends in Covalency for d- and f-Element Metallocene Dichlorides Identified Using Chlorine K-Edge X-ray Absorption Spectroscopy and Time-Dependent Density Functional Theory. *J. Am. Chem. Soc.* **2009**, *131*, 12125–12136.
- [14] Islam, M. A.; Autillo, M.; Guérin, L.; Tamain, C.; Moisy, P.; Bolvin, H.; Berthon, C. Dipolar and contact paramagnetic NMR chemical shifts in An(IV) complexes with dipicolinic acid derivatives. *Inorg. Chem.* **2022**, *61*, 10329–10341.
- [15] Farnan, I.; Berthon, C. SPR-Nuclear Magnetic Resonance. In *Applications of NMR in nuclear chemistry*, Vol. 45; Ramesh, V., Ed.; Royal Society of Chemistry: , 2016; Chapter 3.
- [16] Schnaars, D. D.; Gaunt, A. J.; Hayton, T. W.; Jones, M. B.; Kirker, I.; Kaltsoyannis, N.; May, I.; Reilly, S. D.; Scott, B. L.; Wu, G. Bonding trends traversing the tetravalent actinide series: synthesis, structural, and computational analysis of AnIV(Aracnac)–4 complexes (An = Th, U, Np, Pu; Aracnac = ArNC(Ph)CHC(Ph)O; Ar = 3,5-tBu<sub>2</sub>C<sub>6</sub>H<sub>3</sub>). *Inorg. Chem.* **2012**, *51*, 8557–8566.
- [17] Adam, C.; Beele, B. B.; Geist, A.; Mullich, U.; Kaden, P.; Panak, P. J. NMR and TRLFS studies of Ln(III) and An(III) C5-BPP complexes. *Chem. Sci.* **2015**, *6*, 1548–1561.
- [18] Apostolidis, C.; Kovács, A.; Walter, O.; Colineau, E.; Griveau, J.-C.; Morgenstern, A.; Rebizant, J.; Caciuffo, R.; Panak, P. J.; Rabung, T.; Schimmelpfennig, B.; Perfetti, M. Tris-hydridotris(1-pyrazolyl)boratoactinide Complexes: Synthesis, Spectroscopy, Crystal Structure, Bonding Properties and Magnetic Behaviour. *Chem. Eur. J.* **2020**, *26*, 11293–11306.
- [19] Cross, J. N.; Su, J.; Batista, E. R.; Cary, S. K.; Evans, W. J.; Kozimor, S. A.; Mocko, V.; Scott, B. L.; Stein, B. W.; Windorff, C. J.; Yang, P. Covalency in Americium(III) Hexachloride. *J. Am. Chem. Soc.* **2017**, *139*, 8667–8677.
- [20] Su, J.; Batista, E. R.; Boland, K. S.; Bone, S. E.; Bradley, J. A.; Cary, S. K.; Clark, D. L.; Conradson, S. D.; Ditter, A. S.; Kaltsoyannis, N.; Keith, J. M.; Kerridge, A.; Kozimor, S. A.; Löble, M. W.; Martin, R. L.; Minasian, S. G.; Mocko, V.; La Pierre, H. S.; Seidler, G. T.; Shuh, D. K.; Wilkerson, M. P.; Wolfsberg, L. E.; Yang, P. Energy-Degeneracy-Driven Covalency in Actinide Bonding. *J. Am. Chem. Soc.* **2018**, *140*, 17977–17984.
- [21] Autillo, M.; Islam, M. A.; Jung, J.; Pilmé, J.; Galland, N.; Guerin, L.; Moisy, P.; Berthon, C.; Tamain, C.; Bolvin, H. Crystallographic structure and crystal field parameters in the  $[\text{An}^{\text{IV}}(\text{DPA})_3]^{2-}$  series An = Th, U, Np, Pu. *Phys Chem Chem Phys* **2020**, *22*, 14293–14308.
- [22] Tamain, C.; Autillo, M.; Guillaumont, D.; Guérin, L.; Wilson, R. E.; Berthon, C. Structural and bonding analysis in monomeric actinide(IV) oxalate from Th(IV) to Pu(IV): Comparison with the An(IV) nitrate series. *Inorg. Chem.* **2022**, *61*, 12337–12348.
- [23] Islam, M. A.; Berthon, C.; Jung, J.; Bolvin, H. Bonding and Magnetic Trends in the  $[\text{An}^{\text{IV}}(\text{DPA})_3]^{2-}$  Series Compared to the Ln(III) and An(IV) Analogues. *Inorg. Chem.* **2023**, *62*, 17254–17264.
- [24] Kutzelnigg, W. Origin and meaning of the Fermi contact interaction.. *Theoret. Chim. Acta* **1988**, *73*, 173–200.
- [25] Bleaney, B. Nuclear magnetic resonance shifts in solution due to lanthanide ions. *J. Magn. Reson.* **1972**, *8*, 91–100.
- [26] Autillo, M.; Guerin, L.; Dumas, T.; Grigoriev, M. S.; Fedoseev, A. M.; Cammeli, S.; Solari, P. L.; Guilhaud, P.; Moisy, P.; Bolvin, H.; Berthon, C. Insight of the metal-ligand interaction in f elements complexes by paramagnetic NMR spectroscopy. *Chem. Eur. J.* **2019**, *25*, 4435.
- [27] Bolvin, H. Modeling Magnetic Properties of Actinide Complexes. In *Computational Modelling of Molecular Nanomagnets*, Vol. 34; Rajaraman, G., Ed.; Springer International Publishing: Cham, 2023.
- [28] Autillo, M.; Islam, M. A.; Héron, J.; Guérin, L.; Acher, E.; Tamain, C.; Illy, M.-C.; Moisy, P.; Colineau, E.; Griveau, J.-C.; Berthon, C.; Bolvin, H. Temperature dependence of <sup>1</sup>H paramagnetic chemical shifts in actinide complexes, beyond Bleaney’s theory: The An<sup>VI</sup>O<sub>2</sub><sup>2+</sup>-dipicolinic acid complexes (An=Np, Pu) as an example. *Chem. Eur. J.* **2021**, *27*, 7138–7153.
- [29] Poulin-Ponnelle, C.; Duvail, M.; Dumas, T.; Berthon, C. Contribution of Molecular Dynamics in pNMR for the structural determination of An<sup>V</sup> and An<sup>VI</sup> complexes in solution. *Inorg. Chem.* **2022**, *61*, 15895–15909.
- [30] Islam, M. A.; Autillo, M.; Poulin-Ponnelle, C.; Tamain, C.; Bolvin, H.; Berthon, C. Are Actinyl Cations Good Probes for Structure Determination in Solution by NMR?. *Inorg. Chem.* **2023**, *28*, 10916–10927.
- [31] Gendron, F.; Pritchard, B.; Bolvin, H.; Autschbach, J. Magnetic resonance properties of actinyl carbonate complexes and plutonyl(VI)-trinitrate. *Inorg. Chem.* **2014**, *53*, 8577–8592.
- [32] Vonci, M.; Mason, K.; Suturina, E. A.; Frawley, A. T.; Worswick, S. G.; Kuprov, I.; Parker, D.; McInnes, E. J. L.; Chilton, N. F. Rationalization of Anomalous Pseudocontact Shifts and Their Solvent Dependence in a Series of C<sub>3</sub>-Symmetric Lanthanide Complexes. *J. Am. Chem. Soc.* **2017**, *139*, 14166–14172.

- [33] Autillo, M.; Guerin, L.; Dumas, T.; Grigoriev, M. S.; Fedoseev, A. M.; Cammelli, S.; Solari, P. L.; Guillemont, D.; Guilbaud, P.; Moisy, P.; Bolvin, H.; Berthon, C. Insight of the Metal–Ligand Interaction in f-Element Complexes by Paramagnetic NMR Spectroscopy. *Chemistry – A European Journal* **2019**, *25*, 4435–4451.
- [34] Adam, C.; Kaden, P.; Beele, B. B.; Mullich, U.; Trumm, S.; Geist, A.; Panak, P. J.; Denecke, M. A. Evidence for covalence in a N-donor complex of americium(III). *Dalton Trans.* **2013**, *42*, 14068–14074.
- [35] Evans, D. The Determination of the Paramagnetic Susceptibility of Substances in Solution by Nuclear Magnetic Resonance. *J. Chem. Soc.* **1959**, 2003–2005.
- [36] Ryan, J. Species involved in the anion-exchange absorption of quadrivalent actinide nitrates. *J. Phys. Chem.* **1960**, *64*, 1375–1385.
- [37] Reilly, S. D.; Scott, B. L.; Gaunt, A. J. [N(n-Bu)<sub>4</sub>]<sub>2</sub>[Pu(NO<sub>3</sub>)<sub>6</sub>] and [N(n-Bu)<sub>4</sub>]<sub>2</sub>[PuCl<sub>6</sub>]: Starting Materials To Facilitate Nonaqueous Plutonium(IV) Chemistry. *Inorg. Chem.* **2012**, *51*, 9165–9167.
- [38] Sobocinska, M. CCDC 987881: Experimental Crystal Structure Determination. *CSD Communication* **2014**, .
- [39] Errington, R. J.; Izuagie, T.; Waddell, P. G. CCDC 1419654: Experimental Crystal Structure Determination. *CSD Communication* **2015**, .
- [40] Aquilante, F.; Autschbach, J.; Carlson, R. K.; Chibotaru, L. F.; Delcey, M. G.; De Vico, L.; Fdez. Galván, I.; Ferré, N.; Frutos, L. M.; Gagliardi, L.; Garavelli, M.; Giussani, A.; Hoyer, C. E.; Li Manni, G.; Lischka, H.; Ma, D.; Malmqvist, P. Å.; Müller, T.; Nenov, A.; Olivucci, M.; Pedersen, T. B.; Peng, D.; Plasser, F.; Pritchard, B.; Reiher, M.; Rivalta, I.; Schapiro, I.; Segarra-Martí, J.; Stenrup, M.; Truhlar, D. G.; Ungur, L.; Valentini, A.; Vancoillie, S.; Veryazov, V.; Vysotskiy, V. P.; Weingart, O.; Zapata, F.; Lindh, R. Molcas 8: New capabilities for multiconfigurational quantum chemical calculations across the periodic table. *J. Comput. Chem.* **2016**, *37*, 506–541.
- [41] Roos, B. O.; Taylor, P. R.; Siegbahn, P. E. M. A complete active space SCF method (CASSCF) using a density matrix formulated super-CI approach. *Chem. Phys.* **1980**, *48*, 157.
- [42] Andersson, K.; Malmqvist, P.-A.; Roos, B. O.; Sadlej, A. J.; Wolinski, K. Second-order perturbation theory with a CASSCF reference function. *J. Phys. Chem.* **1990**, *94*, 5483.
- [43] Hess, B. A. Relativistic electronic-structure calculations employing a two-component no-pair formalism with external-field projection operators. *Phys. Rev. A* **1986**, *33*, 3742.
- [44] Hess, B. A.; Marian, C. M.; Wahlgren, U.; Gropen, O. A mean-field spin-orbit method applicable to correlated wavefunctions. *Chem. Phys. Lett.* **1996**, *251*, 365.
- [45] Malmqvist, P.-A.; Roos, B. O.; Schimmelpennig, B. The restricted active space (RAS) state interaction approach with spin-orbit coupling. *Chem. Phys. Lett.* **2002**, *357*, 230.
- [46] Vancoillie, S.; Rulíšek, L.; Neese, F.; Pierloot, K. Theoretical description of the structure and magnetic properties of nitroxide-Cu(II)-nitroxide spin triads by means of multiconfigurational ab initio calculations. *J. Phys. Chem. A* **2009**, *113*, 6149–6157.
- [47] Atanasov, M.; Zadrozny, J. M.; Long, J. R.; Neese, F. A theoretical analysis of chemical bonding, vibronic coupling, and magnetic anisotropy in linear iron(ii) complexes with single-molecule magnet behavior. *Chem. Sci.* **2013**, *4*, 139–156.
- [48] Neese, F. Software update: The ORCA program system—Version 5.0. *WIREs Computational Molecular Science* **2022**, *12*, e1606.
- [49] Weigend, F.; Furche, F.; Ahlrichs, R. Gaussian basis sets of quadruple zeta valence quality for atoms H–Kr. *J. Chem. Phys.* **2003**, *119*, 12753–12762.
- [50] Weigend, F.; Ahlrichs, R. Balanced basis sets of split valence triple zeta valence and quadruple zeta valence quality for H to Rn: Design and assessment of accuracy. *Phys. Chem. Chem. Phys.* **2005**, *7*, 3297–3305.
- [51] Stoychev, G. L.; Auer, A. A.; Neese, F. Automatic generation of auxiliary basis sets. *J. Chem. Theory Comput.* **2017**, *13*, 554–562.
- [52] Neese, F. An improvement of the resolution of the identity approximation for the formation of the Coulomb matrix. *J. Comput. Chem.* **2003**, *24*, 1740–1747.
- [53] Reiher, M. Douglas-Kroll-Hess Theory: a relativistic electrons-only theory for chemistry. *Theor. Chem. Acc.* **2006**, *116*, 241–252.
- [54] Ungur, L.; Chibotaru, L. F. Ab Initio crystal field for lanthanides. *Chem. Eur. J.* **2017**, *23*, 3708–3718.
- [55] van Lenthe, E.; Baerends, E. J.; Snijders, J. G. Relativistic regular two-component Hamiltonians. *J. Chem. Phys.* **1993**, *99*, 4597–4610.
- [56] Pantazis, D. A.; Neese, F. All-electron scalar relativistic basis sets for the actinides. *J. Chem. Theory Comput.* **2011**, *7*, 677–684.
- [57] Kutzelnigg, W.; Fleischer, U.; Schindler, M. The IGLO-method: Ab-initio calculation and interpretation of NMR chemical shifts and magnetic susceptibilities. In *NMR Basic Principles and Progress*, Vol. 23; Diehl, P.; Fluck, E.; Gunther, H.; Kosfeld, R.; Seelig, J., Eds.; Springer-Verlag: Heidelberg, Germany, 1990.
- [58] Barone, V. Inclusion of Hartree–Fock exchange in density functional methods. Hyperfine structure of second row atoms and hydrides. *J. Chem. Phys.* **1994**, *101*, 6834–6838.
- [59] Provasi, P. F.; Aucar, G. A.; Sauer, S. P. The effect of lone pairs and electronegativity on the indirect nuclear spin-spin coupling constants in CH<sub>2</sub>X (X = CH<sub>2</sub>, NH, O, S): ab initio calculations using optimized contracted basis sets. *J. Chem. Phys.* **2001**, *115*, 1324–1334.
- [60] Perdew, J. P.; Burke, K.; Ernzerhof, M. Generalized gradient approximation made simple. *Phys. Rev. Lett.* **1996**, *77*, 3865–3868.
- [61] Adamo, C.; Barone, V. Toward reliable adiabatic connection models free from adjustable parameters. *J Chem Phys* **1997**, *274*, 242–250.
- [62] Becke, A. Density–functional thermochemistry. III. The role of exact exchange. *J. Chem. Phys.* **1993**, *98*, 5648–5652.
- [63] Becke, A. A new mixing of Hartree–Fock and local density-functional theories. *J. Chem. Phys.* **1993**, *98*, 1372–1377.
- [64] Yanai, T.; Tew, D. P.; Handy, N. C. A new hybrid exchange–correlation functional using the Coulomb-attenuating method (CAM-B3LYP). *Chem. Phys. Lett.* **2004**, *393*, 51–57.
- [65] Baerends, E. J.; Branchadell, V.; Sodupe, M. Atomic reference energies for density functional calculations. *Chem. Phys. Lett.* **1997**, *265*, 481.
- [66] Rebizant, J.; Apostolidis, C.; Spirlet, M. R.; Andreotti, G. D.; Kanellakopulos, B. Structure of bis(tetraethylammonium) hexanitratouranium(IV). *Acta Cryst.* **1988**, *C44*, 2098–2101.

- [67] Chemcraft, “version 1.8 (build 568b)”, 2020 graphical software for visualization of quantum chemistry computations.
- [68] Autillo, M.; Guerin, L.; Guillaumont, D.; Moisy, P.; Bolvin, H.; Berthon, C. Paramagnetism of Aqueous Actinide Cations. Part II: Theoretical aspects and new measurements on An(IV). *Inorg. Chem.* **2016**, *55*, 12149–12157.
- [69] Atanasov, M.; Ganyushin, D.; Sivalingam, K.; Neese, F. Structure and Bonding, A Modern First-Principles View on Ligand Field Theory Through the Eyes of Correlated Multireference Wavefunctions.. In *Molecular Electronic Structures of Transition Metal Complexes II.*, Vol. 143; Springer, Berlin, Heidelberg: Heidelberg, Germany, 2011.
- [70] Jung, J.; Islam, M. A.; Pecoraro, V. L.; Mallah, T.; Berthon, C.; Bolvin, H. Derivation of lanthanide series crystal field parameters from first principles. *Chem. Eur. J.* **2019**, *25*, 15112–15122.
- [71] Autillo, M.; Guerin, L.; Bolvin, H.; Moisy, P.; Berthon, C. Magnetic susceptibility of actinide(III) cations: Experimental and theoretical study. *Phys. Chem. Chem. Phys.* **2016**, *18*, 6515.
- [72] Autillo, M.; Islam, M. A.; Jung, J.; Pilmé, J.; Galland, N.; Guerin, L.; Berthon, C.; Tamain, C.; Bolvin, H. Crystallographic structure and crystal field parameters in the  $[\text{An}^{\text{IV}}(\text{DPA})_3]^{2-}$  series, An = Th, U, Np, Pu.. *Phys. Chem. Chem. Phys.* **2020**, *22*, 14293–14308.
- [73] Martel, L.; Islam, M. A.; Popa, K.; Vigier, J.-F.; Colineau, E.; Bolvin, H.; Griveau, J.-C. Local structure and magnetism of  $\text{La}_{1-a}\text{M}_a\text{PO}_4$  (M = Sm,  $^{239}\text{Pu}$ ,  $^{241}\text{Am}$ ) explained by experimental and computational analyses. *J. Phys. Chem. C* **2021**, *125*, 22163–22174.
- [74] Beerwerth, J.; Siegel, R.; Hoffmann, L.; Plaga, L. S.; Storek, M.; Bojer, B.; Senker, J.; Hiller, W.; Böhrner, R. Sodium Nitrate: an  $^{17}\text{O}$  NMR Study. *Appl. Magn. Reson.* **2020**, 597–620.
- [75] Hung, I.; Wu, G.; Gan, Z. Second-order quadrupolar line shapes under molecular dynamics: An additional transition in the extremely fast regime. *Solid State Nucl. Magn. Reson.* **2017**, *84*, 14–19 Solid-state NMR spectroscopy of Quadrupolar Nuclei.
- [76] Elliott, N. A Redetermination of the Carbon—Oxygen Distance in Calcite and the Nitrogen—Oxygen Distance in Sodium Nitrate. *J. Am. Chem. Soc.* **1937**, *59*, 1380–1382.
- [77] McConnell, H. M.; Robertson, R. E. Isotropic Nuclear Resonance Shifts. *J. Chem. Phys.* **1958**, *29*, 1361–1365.
- [78] Bertini, I.; Luchinat, C.; Parigi, G. Magnetic susceptibility in paramagnetic NMR. *Prog. Nucl. Mag. Res. Spectrosc.* **2002**, *40*, 249.
- [79] Fratiello, A.; Kubo-Anderson, V.; Azimi, S.; Chavez, O.; Laghaei, F.; Perrigan, R. A direct nitrogen-15 NMR study of praseodymium(III)-nitrate complex formation in aqueous solvent mixtures. *J. Solution Chem.* **1993**, *22*, 519–538.
- [80] Fratiello, A.; Kubo-Anderson, V.; Lee, D.; Perrigan, R.; Wong, K. A Direct Carbon-13 and Nitrogen-15 NMR Study of Samarium(III)–Isothiocyanate Complexation in Aqueous Solvent Mixtures. *J. Solution Chem.* **1998**, *27*, 581–600.
- [81] Golding, R. The theory of the temperature dependence of NMR spectra of paramagnetic octahedral complexes. *Mol. Phys.* **1964**, *8*, 561–566.
- [82] Kurland, R. J.; McGarvey, B. R. Isotropic NMR shifts in transition metal complexes: The calculation of the fermi contact and pseudocontact terms. *J. Magn. Reson.* **1970**, *2*, 286 – 301.
- [83] Van den Heuvel, W.; Soncini, A. NMR chemical shift in an electronic state with arbitrary degeneracy. *Phys. Rev. Lett.* **2012**, *109*, 073001.
- [84] Vaara, J.; Rouf, S. A.; Mareš, J. Magnetic Couplings in the Chemical Shift of Paramagnetic NMR. *J. Chem. Theory Comput.* **2015**, *11*, 4840–4849.
- [85] Gendron, F.; Sharkas, K.; Autschbach, J. Calculating NMR chemical shifts for paramagnetic metal complexes from first-principles. *J. Phys. Chem. Lett.* **2015**, *6*, 2183–2188.
- [86] Sharkas, K.; Pritchard, B.; Autschbach, J. Effects of spin-orbit coupling on electron-nucleus hyperfine coupling calculated at the restricted active space level for Kramers doublets. *J. Chem. Theory Comput.* **2015**, *11*, 538.
- [87] Gendron, F.; Autschbach, J. Ligand NMR chemical shift calculations for paramagnetic metal complexes:  $5f^1$  vs.  $5f^2$  actinides. *J. Chem. Theory Comput.* **2016**, *12*, 5309–5321.
- [88] Birnoschi, L.; Chilton, N. F. Hyperion: A new computational tool for relativistic ab initio hyperfine coupling. *J. Chem. Theory Comput.* **2022**, *18*, 4719–4732.
- [89] Golding, R.; Halton, M. P. A theoretical study of the  $^{14}\text{N}$  and  $^{17}\text{O}$  NMR shifts in lanthanide complexes. *Aust. J. Chem.* **1972**, *25*, 2577–2581.
- [90] Pinkerton, A. A.; Rossier, M.; Spiliadis, S. Lanthanide-induced contact shifts. the average electron spin polarization, theory and experiment. *J. Magn. Reson.* **1985**, *64*, 420–425.
- [91] Sergentu, D.-C.; Gendron, F.; Autschbach, J. Similar ligand-metal bonding for transition metals and actinides?  $5f^1$  U(C7H7)2-versus  $3d^n$  metallocenes. *Chem. Sci.* **2018**, *9*, 6292–6306.
- [92] Fermi, E. Über die magnetischen Momente der Atomkerne. *Z. Physik* **1930**, *60*, 320–333.
- [93] Pell, A. J.; Pintacuda, G.; Grey, C. P. Paramagnetic NMR in solution and the solid state. *Prog. Nucl. Mag. Res. Spectrosc.* **2019**, *111*, 1–271.
- [94] Neese, F. Theoretical study of ligand superhyperfine structure. Application to Cu(II) complexes. *J. Phys. Chem. A* **2001**, *105*, 4290–4299.
- [95] Aquino, F.; Pritchard, B.; Autschbach, J. Scalar relativistic computations and localized orbital analyses of nuclear hyperfine coupling and paramagnetic NMR chemical shifts. *J. Chem. Theory Comput.* **2012**, *8*, 598–609.
- [96] Hedegård, E. D.; Kongsted, J.; Sauer, S. P. A. Validating and analyzing EPR hyperfine coupling constants with Density Functional Theory. *J. Chem. Theory Comput.* **2013**, *9*, 2380–2388.
- [97] Yamamoto, K.; Gordon, C. P.; Liao, W.-C.; Copéret, C.; Raynaud, C.; Eisenstein, O. Orbital analysis of Carbon-13 chemical shift tensors reveals patterns to distinguish Fischer and Schrock carbenes. *Angew. Chem. Int. Ed.* **2017**, *56*, 10127–10131.
- [98] Abragam, A.; Bleaney, B. *Electronic paramagnetic resonance of transition ions*; Clarendon Press: Oxford, 1970.
- [99] Munzarová, M. L.; Kubáček, P.; Kaupp, M. Mechanisms of EPR hyperfine coupling in transition metal complexes. *J. Am. Chem. Soc.* **2000**, *122*, 11900–11913.
- [100] Liimatainen, H.; Pennanen, T. O.; Vaara, J.  $^1\text{H}$  chemical shifts in nonaxial, paramagnetic chromium(III) complexes — Application of novel pNMR shift theory. *Canadian Journal of Chemistry* **2009**, *87*, 954–964.
- [101] Pritchard, B.; Autschbach, J. Theoretical Investigation of Paramagnetic NMR Shifts in Transition Metal Acetylacetonato Complexes: Analysis of Signs, Magnitudes, and the Role of the Covalency of Ligand–Metal Bonding. *Inorganic Chemistry* **2012**, *51*, 8340–8351 PMID: 22835057.

- [102] Islam, M. A.; Pell, A. J. Delving into theoretical and computational considerations for accurate calculation of chemical shifts in paramagnetic transition metal systems using quantum chemical methods. *Phys. Chem. Chem. Phys.* **2024**, –.